crystals

Article
Phononic Crystal Coupled Mie Structure for Acoustic Amplification

Jianning Han *, Guodong Hao, Wenying Yang and Xinsa Zhao *

School of Information and Communication Engineering, North University of China, Taiyuan 030051, China; adeneogdhao@163.com (G.H.); zbduoyuanduomo@163.com (W.Y.)
* Correspondence: hanjn46@nuc.edu.cn (J.H.); xinsazhao@163.com (X.Z.)

Abstract: In the field of industrial structure detection, acoustic signals have been pivotal. A cost-effective and highly sensitive acoustic monitoring system that can enhance weak acoustic signals has always been an interesting topic in many research fields. However, environmental noise signals have consistently hindered the improvement of the signal-to-noise ratio (SNR) of traditional acoustic systems. In this work, we propose a structure (PC-Mie) that couples phononic crystal (PC) point defects and Mie resonance structures (Mies) to enhance weak effective signals from complex environments. Numerical simulations have confirmed that the PC-Mie exhibits superior sound pressure enhancement performance compared to each individual PC point defect and Mies. Moreover, the capability to amplify the sound pressure amplitude is related to the angle and position of the Mies at the center position. Simultaneously, the PC-Mie has a narrower bandwidth, giving the structure stronger frequency selectivity. Finally, the experiment proves that PC-Mie can function as an enhanced acoustic device or sensor to detect harmonic signals, verifying the validity of the PC-Mie structure for acoustically enhanced perception. Both numerical and experimental studies demonstrate that the PC-Mie can effectively enhance the energy of specific sound frequencies in complex air environments, making it suitable for collecting high-sensitivity acoustic signals. This research has significant implications for the development of weak acoustic signal detection technology and the application of self-powered sensors.

Keywords: phononic crystals; Mie resonance structure; acoustic metamaterials; acoustic enhancement

check for updates

Citation: Han, J.; Hao, G.; Yang, W.; Zhao, X. Phononic Crystal Coupled Mie Structure for Acoustic Amplification. *Crystals* **2023**, *13*, 1196. https://doi.org/10.3390/cryst13081196

Academic Editors: Jihong Ma and Yanyu Chen

Received: 20 July 2023
Revised: 29 July 2023
Accepted: 31 July 2023
Published: 1 August 2023

1. Introduction

Acoustic sensing-based monitoring systems are crucial in various applications, including structural health monitoring [1,2]. Acoustic sensor devices with high signal-to-noise ratio (SNR) are the key to acoustic monitoring systems [3,4]. Typically, traditional acoustic sensing methods rely on conventional electroacoustic sensor compositions [5–7]. In recent years, there has been some progress in breaking through the signal-to-noise ratio (SNR) of electro-acoustic sensors. However, due to the sensing threshold of these sensors, many acoustic signals may be lost when converting limited sound energy into electrical energy. Therefore, new sensing modalities need to be developed to break through the limitations of detection and collection of weak acoustic signals.

Over the past two decades, researchers have shown considerable interest in the use of acoustically artificial structures to achieve anomalous acoustic properties not found in conventional acoustic materials [8–15]. A phononic crystal (PC) [16–20] is an acoustic metamaterial comprised of periodically repeating unit cells with a lattice constant comparable to the wavelength range [21]. The band gap and the refractive index [22] exhibited by the equivalent medium are the main properties of PC. A band gap is a certain frequency range in which waves are prohibited from propagating through a PC [23]. Band gaps are part of the category of evanescent waves. Within the band gap, the PC experiences a evanescent wave, with its amplitude exponentially decaying in the direction of the incident wave. Numerous studies have focused on enhancing the localization of acoustic energy through defects in PCs [24–27]. Refs. [28,29] investigated the localization of acoustic energy in one-dimensional and two-dimensional band-defect PCs. To investigate the effect of defect configuration, Refs. [30,31] gave numerical methods to examine the variation of defect band and energy localization properties with filling fraction and relative position of circular inclusions within the defect, respectively. Qi et al. [32] developed an acoustic energy acquisition system based on single-defect planar PnC. To reduce the defect band frequencies, Oudich et al. [33] proposed a subwavelength metamaterial for tunable and efficient subwavelength acoustic energy harvesting through an array of mass-spring resonators with square surfaces composed of aluminum plates.

In addition, metamaterials with high refractive index media can be used to fabricate coil structures, which helps to reduce the size of the metamaterial structure. In coiled-coil structures, known as locally resonant acoustic metamaterials (LAMMs), acoustic waves are forced to propagate through the channel system, significantly increasing the total propagation time and therefore leading to low sound velocities and high refractive indices [34], while having high effective mass densities and bulk moduli. Recently, Mie resonance structures [35–38] have been constructed using combined coiled structures to achieve acoustic signal direction sensing and acoustically omnidirectional antennas [37]. In conclusion, both PC defect state structure and Mie resonant structured metamaterials have demonstrated excellent performance in controlling acoustic wave propagation and spatial distribution of acoustic energy. In the field of weak acoustic signal perception, the combination of PC point defects and Mies may enhance acoustic energy enhancement. However, there has been little research on coupled structures for acoustic enhancement sensing thus far.

To realize broadband acoustically enhanced sensing, a coupling model (PC-Mie) between a phonon crystal (PC) point defects and a Mie resonant structure (Mies) is designed in this study. Compared to conventional PC or Mies, this model provides greater amplification of acoustic energy amplitude for specific frequencies. Furthermore, the multiple structural features of the PC-Mie model enable it to be reasonably tuned for weak acoustic perception scenarios at different frequencies.

The paper is organized as follows. Following the introduction, Section 2 derives the structural design of the proposed metamaterial model through numerical calculations. Section 3 presents the mechanistic analysis of the PC band properties and the Mies. In Section 4, finite element simulations of the model are performed to verify the properties of the designed metamaterial by comparing the acoustic energy harvesting performance of the PC point defects, the Mies, and the PC-Mie. Additionally, the section investigates the effects of angular and positional offsets of the Mies on the acoustic field gain. In Section 5, an experimental study is conducted to investigate the acoustic enhancement properties of the PC-Mie based detection method for harmonic signals. Finally, Section 6 presents the conclusions of the study.

2. Model Structural Design

The overall structure of the designed PC-Mie is shown in Figure 1a, which consists of a square lattice array of 5×5 cylindrical columns and the center removed to accommodate a cylindrical, coupled Mies. The phononic crystal is constructed using acrylic materials and has a height of 90 mm. Figure 1b provides a top view of the PC-Mie, while Figure 1c offers an enlarged view of the Mies within the PC-Mie metamaterial, with relevant dimensional parameters marked. The structure consists of four coiled structures fan-wrapped around a circular hard core. The Mies slit spacing is a, the grid width is t, the inner core radius is R_1, the outermost radius is R_2, and the opening and backbone angles are set to θ_1 and θ_2, respectively. To increase the minimum threshold for sound pressure perception in the PC-Mie system, phononic crystals are arranged around the Mies such that they can concentrate the acoustic energy locally around the Mies at its resonant frequency. The designed phononic crystal consists of a cylindrical rigid structure with a radius of e, embedded within an air lattice with an edge length of c, as shown in Figure 1d. The parameters selected here are all suitable values within a certain range to facilitate processing and experimental measurements. All parameters are summarized and listed in Table 1.

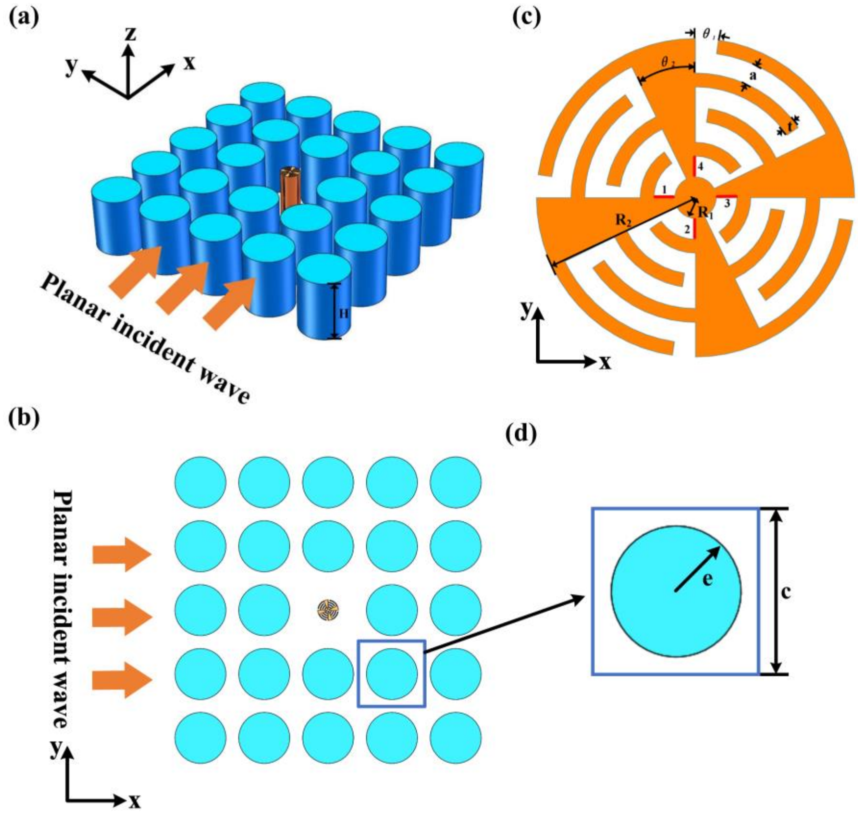

Figure 1. (**a**) Overall structure of PC-Mie; (**b**) top view of PC-Mie; (**c**) enlarged view of the Mies; (**d**) PCs unit.

Table 1. Summary of geometric characteristic parameters for PC-Mies.

Parameters	a	t	H	θ_1	θ_2	R_1	R_2	c	e
Values (mm/deg)	2.45	1	90	8.6	26	2.1	16.1	100	40

3. Theoretical Analysis

3.1. Phononic Crystal Frequency Band Characterization

The PC array structure consists of a square lattice array with cylindrical columns inside. At this time, the cylinders are periodically deposited in the air as rigid body boundaries. Its acoustic properties are theoretically investigated using the Bloch–Floquet theorem. The acoustic initial equation can be written as

$$\nabla \cdot \left(\frac{1}{\rho(r)} \nabla p(r) \right) + \frac{\omega^2}{\rho(r)c^2(r)} = 0 \tag{1}$$

where r is the position vector, $\rho(r)$ is the mass density, $p(r)$ is the sound pressure field, $c(r)$ is the speed of sound in air, and ω is the angular frequency. $p(r)$ can be expanded into Fourier exponential form

$$p(r) = e^{ik \cdot r - \omega t} \sum_{G_n} \Phi_k(G_n) \cdot e^{iG_n \cdot r} \tag{2}$$

where k is a Bloch wave vector in the first integrable Brillouin zone (BZ), and G_n is a reciprocal inverse lattice vector. The band structure can be built by solving Equation (1) for ω, which is a function of the wave vector k

$$\nabla \cdot \left(-\frac{1}{\rho}\nabla p_0\right) - \frac{\omega^2 p_0}{\rho(r)c^2(r)} = 0 \tag{3}$$

The pressure field distribution can be obtained by solving Equation (3). When a unit cell is removed from a perfect PC, a PC point defect is created, which acts as a resonant cavity. Acoustic waves that propagate at the resonant frequency can be confined within the defect region, subsequently leading to a marked increase in energy density.

3.2. Mechanism of the Mies

The sound waves are forced to propagate along a distinctive "Z" shaped path in a sector of the Mies coiled around the structure. This specialized propagation route induces an increase in the relative refractive index of the sector. As a result, this facilitates a significant amplification of sound energy. The acoustic energy is reflected several times in the fan-shaped coiled structure, focusing the incident acoustic waves near the intrinsic frequency inside the coiled structure, where the energy localization is improved [22]. To make the Mies match the defective state PCs, after determining the structural radius of a suitable Mies, the resonant frequency of the structure is modified by changing the sector angle θ_2 of the main stem of the Mies. In general, the incident signal resonant frequency of the Mies is

$$\omega_n = (2n+1)\omega_0 \tag{4}$$

where

$$\omega_0 = c_o \cdot \pi/(2L) \tag{5}$$

c_0 represents the speed of sound in air, n is the order of the overtone, and L denotes the total distance traversed by the sound within the coiled structure. The larger the sector angle θ_2 is, the shorter the total sound propagation distance L in the coiled structure and the higher the resonant frequency chosen for that structure are. Conversely, a smaller sector angle θ_2 leads to a longer sound propagation distance L within the structure, and consequently, a lower resonant frequency is selected for such a structure [38]. In this study, the resonant frequency of Mie is controlled by modulating the geometrical parameters to match the resonant frequency of the PC point defect, thus achieving acoustic energy enhancement.

The resonant coupling between the PC point defect and the Mies reaches its peak strength when the resonant frequencies of both structures align perfectly. Firstly, the acoustic energy is concentrated in the defect region through the PC, increasing the density of acoustic energy where the Mies is located. Secondly, the Mies can further amplify the sound pressure at the defect by interacting with the waves within the defective structure at the PC point through the superposition of the acoustic pressure on all four sides. Hence, the PC-Mie exhibits superior acoustic enhancement compared to either PC or Mies. In addition, the strongest resonant coupling effect results in a narrower resonance bandwidth, giving the structure exceptional frequency selectivity.

4. Simulation Analysis of Models

4.1. Analysis of the Acoustic Energy Harvesting Performance of PC Point Defect, Mies, and PC-Mies

To accurately characterize the acoustic response of the metamaterial, a two-dimensional structure is constructed in the acoustics module (pressure acoustics) of COMSOL Multiphysics v6.0, for which numerical calculations are performed. As the structure is in an air environment and can be considered as a rigid body, the boundary of the structure is set as a hard acoustic field boundary. The incident acoustic wave is incident from the left side using a plane wave with an amplitude of 1 Pa. A perfectly matched layer (PML) is added around the area to absorb the reflected acoustic waves. To observe the acoustic enhancement effect of the constructed acoustic metamaterial, the measured location points are chosen as probe locations for acquiring pressure data. The positions of these four probe points are indicated by the red markers in Figure 1c. The pressure gain value serves as a crucial metric for evaluating the acoustic enhancement effect. The pressure gain PG is defined by the equation PG = PM/PF [39]. PM represents the sound pressure amplitude within the PC, while PF denotes the sound pressure amplitude in free space without the PC.

At first, the PC defect state and Mies are analyzed separately. Figure 2a illustrates the energy band gap diagram of the PC defect state. It distinctly exhibits a forbidden band spanning from 1792 Hz to 2212 Hz. Within this frequency range, it is reasonable to assume that the acoustic energy is localized at the PC defect location, giving rise to various resonance phenomena. Therefore, the probe is placed at the central location of the PC defect. The absolute acoustic pressure frequency response of the structure at the defect point location is plotted (as shown in Figure 2b). The maximum pressure gain value, located at the resonance frequency of 1982 Hz, is found to be 4.6. Figure 2c depicts the distribution of resonant frequency sound pressure generated by the PC at the defect location, further indicating that the acoustic energy can be confined to the PC point defect region. This phenomenon can be attributed to the influence of the defect structure on the band gap of the original phononic crystal, which alters the periodicity of the local structure of the phononic crystal. Acoustic waves experience multiple reflections and localized resonance at point defects, leading to resonance peaks in the transmission characteristic curve in the bandgap frequency range [40]. Therefore, the presence of PC defective state structure exhibits excellent transmission properties for acoustic waves, alongside notable acoustic energy aggregation enhancement characteristics.

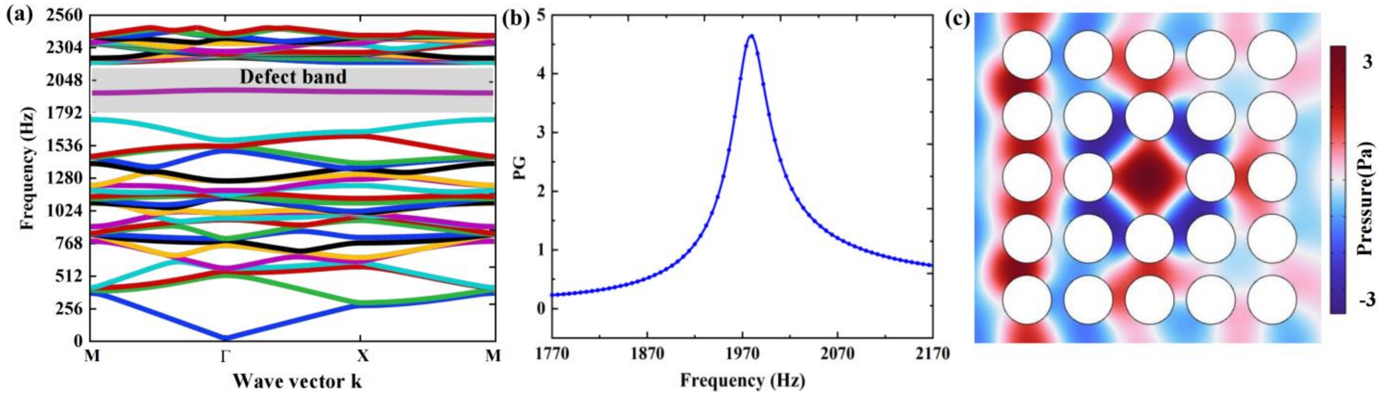

Figure 2. (**a**) Energy band diagram of PCs; (**b**) absolute sound pressure frequency response at the central position of PCs; (**c**) distribution of resonance frequency sound pressure generated by the PCs at the defect position.

The resonant frequency of the Mies is matched with the resonant frequency of the PCs described above by changing the characteristics of the structure. The energy bandgap diagram of the Mies is obtained after numerical calculations, as shown in Figure 3a. The diagram reveals that the structure possesses the property of localizing the acoustic energy within itself in the frequency range of 1950 Hz to 2062 Hz. Figure 3b provides a partially localized enlarged view of the bandgap map, revealing that the structure has two eigenfrequencies in this range near 1982 Hz and 1987 Hz, respectively. Therefore, the resonance frequency of the Mies exists in this frequency range. The absolute acoustic pressure frequency response of the structure at the four probe positions is plotted in Figure 3c. Figure 3d demonstrates that the value of the maximum pressure gain at the resonance frequency of 1982 Hz is 179.2. Apparently, the acoustic energy is confined within the cavity of the Mies.

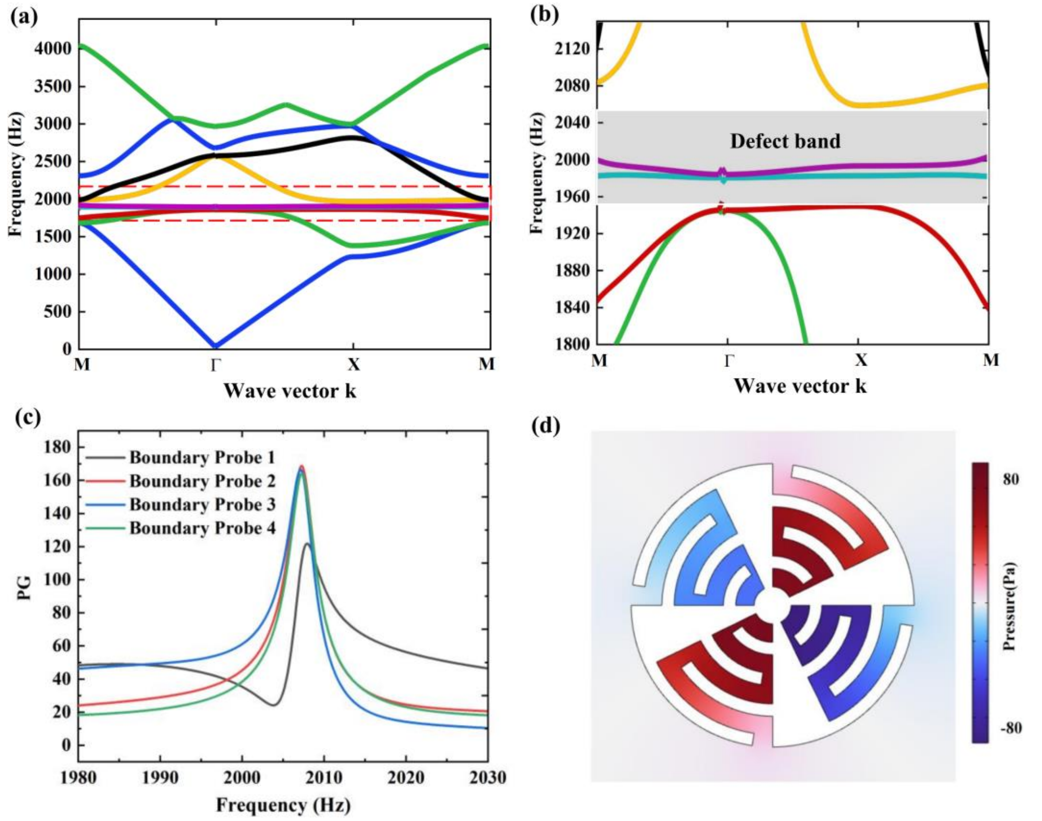

Figure 3. (**a**) Energy band diagram of Mies; (**b**) localized magnification of the energy band of Mies; (**c**) absolute acoustic pressure frequency response at the four probe positions of Mies; (**d**) distribution of acoustic pressure at resonance frequencies generated by the four probe positions of Mies.

The Mies is placed in the center of the defect position of the PC. The energy bandgap diagram, resulting from the addition of the Mies to the defect state PC, is illustrated in Figure 4a. It is evident that a clear defect band gap exists at the frequency position near 1982 Hz. By positioning the probes at the center of the Mies, the frequency response diagrams of the PC-Mies at four probe positions are obtained and depicted in Figure 4b. The structure achieves resonance pressure gains of 703, 700, 698, and 689 at the frequency of 1980.4 Hz, respectively, when an incident acoustic wave is introduced from the left side. The pressure acoustic field distributions of the PC-Mies, at the time when the probe possesses the strongest pressure, are further illustrated in Figure 4c,d. The pressure gain experiences further amplification, a phenomenon that can be explained by observing the energy bandgap diagram. Given that the defect bandgap displays a minor variation in the operating frequency in different acoustic wave incidence directions, the Mies operate at 1976 Hz when the incident acoustic wave is introduced from the left side, while the PC defect state operates at 1982 Hz. When two structures operate at similar frequencies, the bandwidths intersect, and the sound field gains greater gain capability in the intersecting frequency range, resulting in the strongest acoustic resonance coupling occurs between them. Thus, the coupled resonant structure has greater acoustic pressure amplification performance than each individual structure.

Additionally, the external field of the structure is analyzed by placing the probe at the left incident acoustic wave port. It is positioned 400 mm away from the center of the PC-Mie structure and passes through the structure. The acoustic pressure gains detected by the probe, with and without the adding the Mies, are found to be 0.36 and 0.78, respectively. By comparison, the PC-Mies is found to have a lower acoustic transmittance than the defect state PCs. This observation indicates that the PC-Mies also exhibits outstanding performance in the application of frequency-specific acoustic isolation.

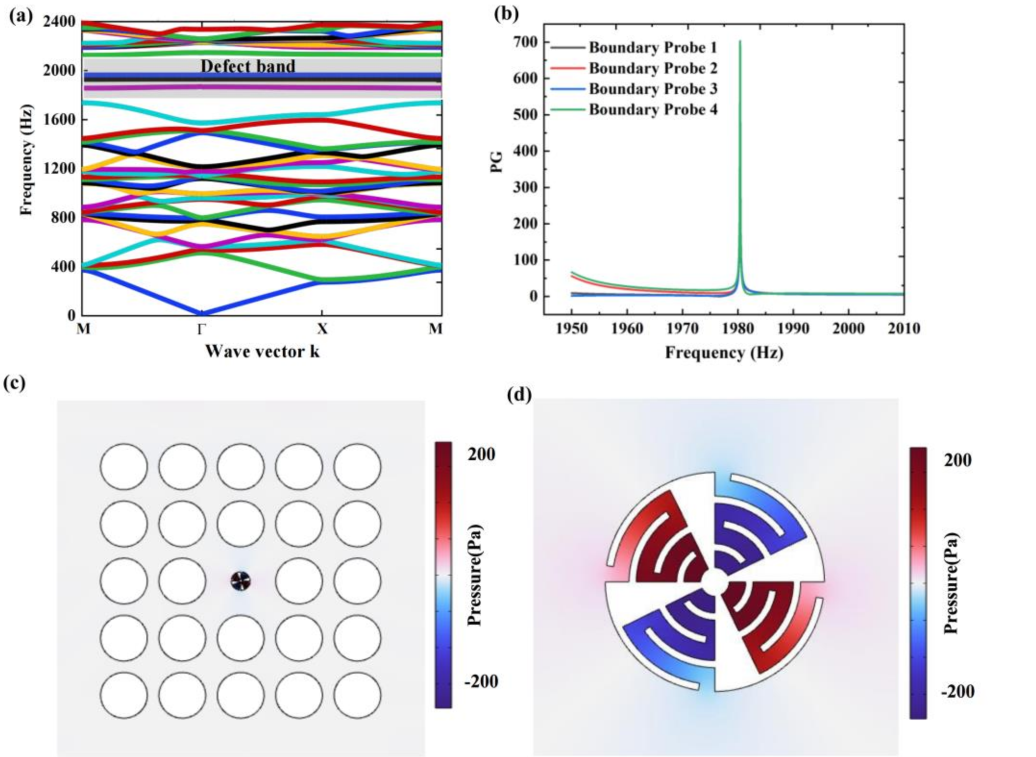

Figure 4. (**a**) Energy band diagram of PC-Mies. (**b**) Frequency correspondence diagram of PC-Mies. (**c**) PC-Mie sound pressure distribution map (**d**) PC-Mie sound pressure distribution localized map.

4.2. Analysis of the Effect of the Angle of the Mies in the PC Point Defects on the Sound Field Gain

To verify the directionality of the PC-Mies in acoustic enhancement performance, the orientation of the Mies is rotated while keeping the PC defect state orientation fixed, as depicted in Figure 5a. When the incidence angle β of the plane wave holds constant, the directional angle θ_m is altered by rotating the Mies. Using the Mies circular position gap edge position as the probe point, the Mies is rotated in steps of 15 deg to obtain the frequency response maps of the Mies at various angles. Under the assumption of ignoring the metamaterial boundary impedance and considering adiabatic conditions, as shown in Figure 5b–f, the maximum sound pressure gain is 97 times at the initial position with a 15-degree angular offset of the Mies. At an angular offset of 30 degrees from the initial position of Mies, the maximum sound pressure gain is found to be 27 times. When the angular offset is increased to 45 degrees, the maximum sound pressure gain exhibits a gain of 18 times. Interestingly, beyond a 45-degree angle, the gain trend begins to rise again. At an offset of 60 degrees, the gain capacity reaches 55.7 times, and at 75 degrees, it achieves a gain capacity of 96.8 times. The results demonstrate that, in addition to the acoustic enhancement of the PC-Mies, there is a significant directional response of the angle of the internal Mies, due to the sensitivity of the Mies to the angle of incidence of the acoustic wave. Theoretically, the PC point defect is insensitive to the directional response. By placing the Mies at the cavity center of the PC point defect, a potent acoustic resonance mode is created within the resulting PC-Mie structure. This phenomenon can be attributed to the powerful acoustic coupling between the resonance mode of the Mies and the defect resonance mode of the PC point defect. Therefore, this arrangement can significantly enhance the wave directivity.

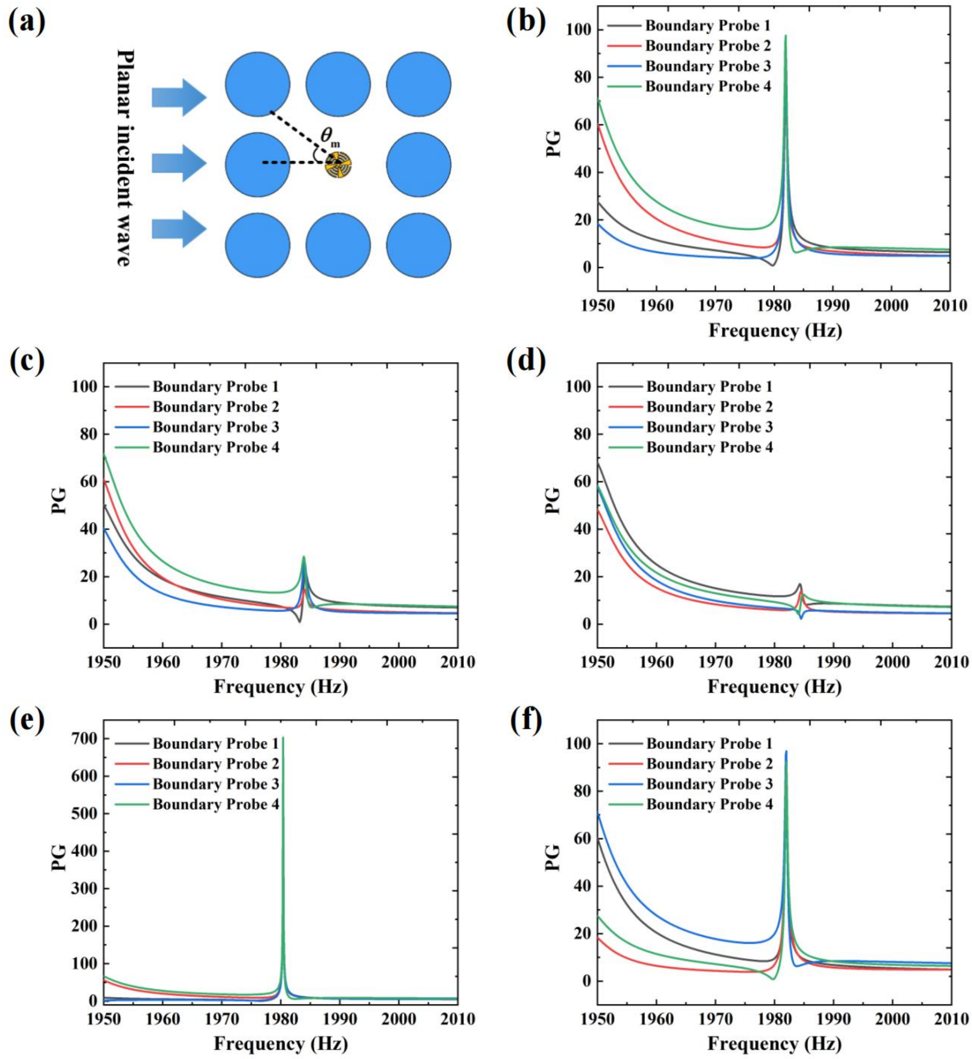

Figure 5. Results of the effect of angle of Mies on sound field gain. (**a**) Schematic diagram of angle rotation; (**b**–**f**) frequency response plots of Mies at different angles: (**b**) 15 degrees; (**c**) 30 degrees; (**d**) 45 degrees; (**e**) 60 degrees; (**f**) 75 degrees.

4.3. Analysis of the Effect of the Location of the Mies in the PC Point Defects on the Sound Field Gain

To verify the effect of Mies location on the robustness of PC-Mie acoustic energy enhancement, the position of the Mies is varied by keeping the defect state orientation constant. By using the edge of the circular position gap of the Mie resonant structure as the probe point, and keeping the incident acoustic wave fixed to occur from the left side of the PC-Mie structure, the frequency response map of the PC-Mie structure is observed. Figure 6a presents a schematic of the offset position of the Mies. Taking the center of the Mie structure as the initial position, the new position is acquired in the frequency domain by sequentially translating to the left in steps of d = 2 mm. Figure 6b–f illustrate the frequency response of the PC-Mies structure corresponding to each translation distance of the Mies.

Under the assumptions of ignoring boundary impedance and adiabatic conditions, the PC-Mie structure has a maximum sound pressure gain of 652 times at 2 mm translation of the Mies. When the shift is increased to 4 mm, the gain decreases to 376.7 times. With a shift of 6 mm, the gain falls further to 326.5 times. A shift of 8 mm results in a gain of 264.4 times. Lastly, when the Mies is displaced by 10 mm, the gain stands at 243.8 times. It can be found that the closer the Mies is to the center of the PC defect state, the higher the sound pressure gain capacity. Conversely, as the Mie structure is displaced further from the center of the

PC defect state, the gain capacity decreases. Furthermore, as the distance increases, the rate of change in the gain capacity also decreases. In conclusion, the inclusion of the equivalent medium Mies significantly amplifies the sound pressure of the localized environment. The gain multiplier of the total sound field is the gain multiplication of the Mie structure at that frequency by the gain multiplier of the constructed localized sound field environment compared to the free field. The performance of the Mies in terms of sound pressure gain can also be controlled by adjusting the position of the Mies, utilizing the position-adjustable feature of the structure that corresponds to different gain capabilities.

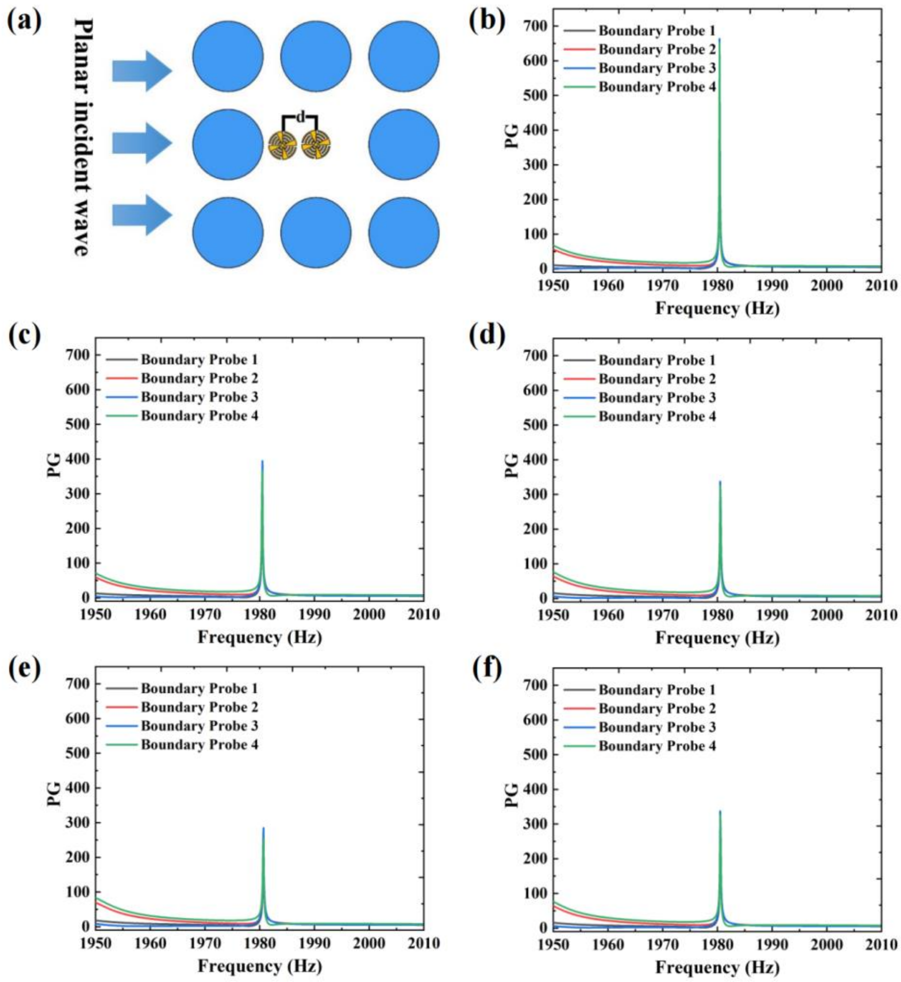

Figure 6. Results of the effect of the position of the Mies on the sound field gain. (**a**) Schematic diagram of the position shift; (**b**–**f**) frequency response plots of the PC-Mies at different positions: (**b**) 2 mm left translation; (**c**) 4 mm left translation; (**d**) 6 mm left translation; (**e**) 8 mm left translation; (**f**) 10 mm left translation.

5. Experimental Investigation of Harmonic Signal Detection

To evaluate the perceptual performance of the proposed PC-Mies when processing specialized signals, this paper conducted a test. A sample of the Mies is fabricated utilizing 3D printing technology and photoresist materials, with a height of 90 mm. The phononic crystal is constructed using acrylic materials and has a height of 90 mm. To visually distinguish it from the surrounding environment and enhance observational clarity, we inject dye into the crystal. The harmonic signal is remotely outputted through an upper computer system to control the speaker. The acoustic measurement device used in this study is a MEMS-MIC (model: S15OT421-005) with a sensitivity of −42 dB and an amplification gain of 66. This device is positioned at the edge of the central cavity to detect and analyze the acoustic signals. In the absence of acoustic signals, the output voltage of the MEMS-MIC fluctuates around 1.5 V. The MEMS-MIC is positioned at the inner edge of the PC-Mies so that in the testing environment, the probe's inclusion minimizes any disruption to the internal sound pressure distribution of the metamaterial. The distance between the speaker and the measurement point is D = 0.45 m in the test environment setup (Figure 7).

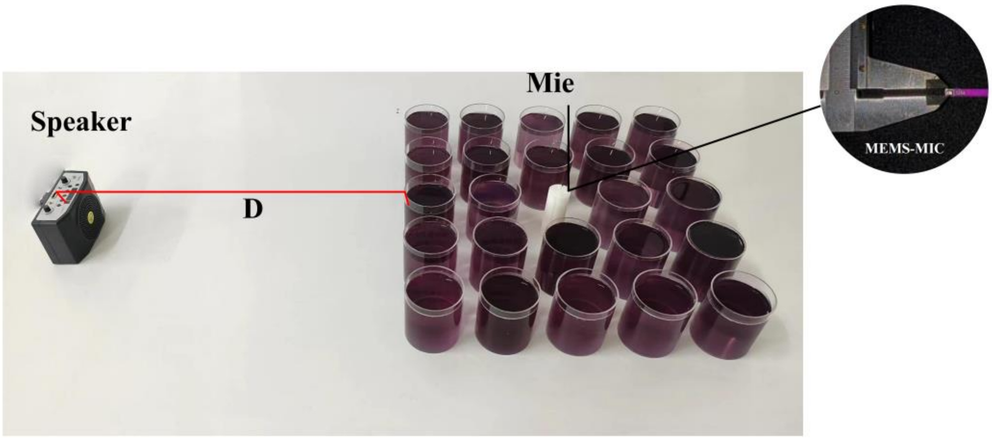

Figure 7. Schematic diagram of the experimental setup.

In the context of a factory environment, accurate detection of mechanical bearing faults is crucial for maintaining production safety [41,42]. The key to effective fault feature extraction lies in enhancing the Signal-to-Noise Ratio (SNR) of the bearing fault signal. This can be achieved by either filtering out the noise or amplifying the target signal. In this study, we simulate the sound of mechanical bearing malfunctions using a speaker to output harmonic signals. The harmonic signal is

$$P(t) = 10 \times \cos(2\pi \times f_1 \times t) + \cos(2\pi \times f_0 \times t) \tag{6}$$

where the target frequency f_0 is set as 1982 Hz, and the disturbance frequency f_1 is set as 1200 Hz. Figure 8a illustrates the frequency domain analysis of the original harmonic signal. The collected acoustic signals are analyzed in the frequency domain, and the frequency spectra obtained from the calculations are normalized. Figure 8b illustrates the harmonic signal spectrum of the PC point defect. The PC point defect has a significant gain effect on the signal amplitude of the target frequency component. Figure 8c–f display the spectrum distribution at four probe positions of the PC-Mies. When compared to the spectrum obtained from the PC point defect, the curves derived from the PC-Mies feature prominent peaks. These structures, specifically the PC-Mies, may have a robust response near the resonant frequency f_0 = 1982 Hz, even if the incident sound wave is non-stationary in frequency. The PC-Mies exhibits a notably stronger gain effect on the signal amplitude of the target frequency component compared with the individual PC point defect. Furthermore, it is found that the signal amplitudes detected at the four probe positions are nearly identical, which is conducive to extracting monitoring target signals against a wide area.

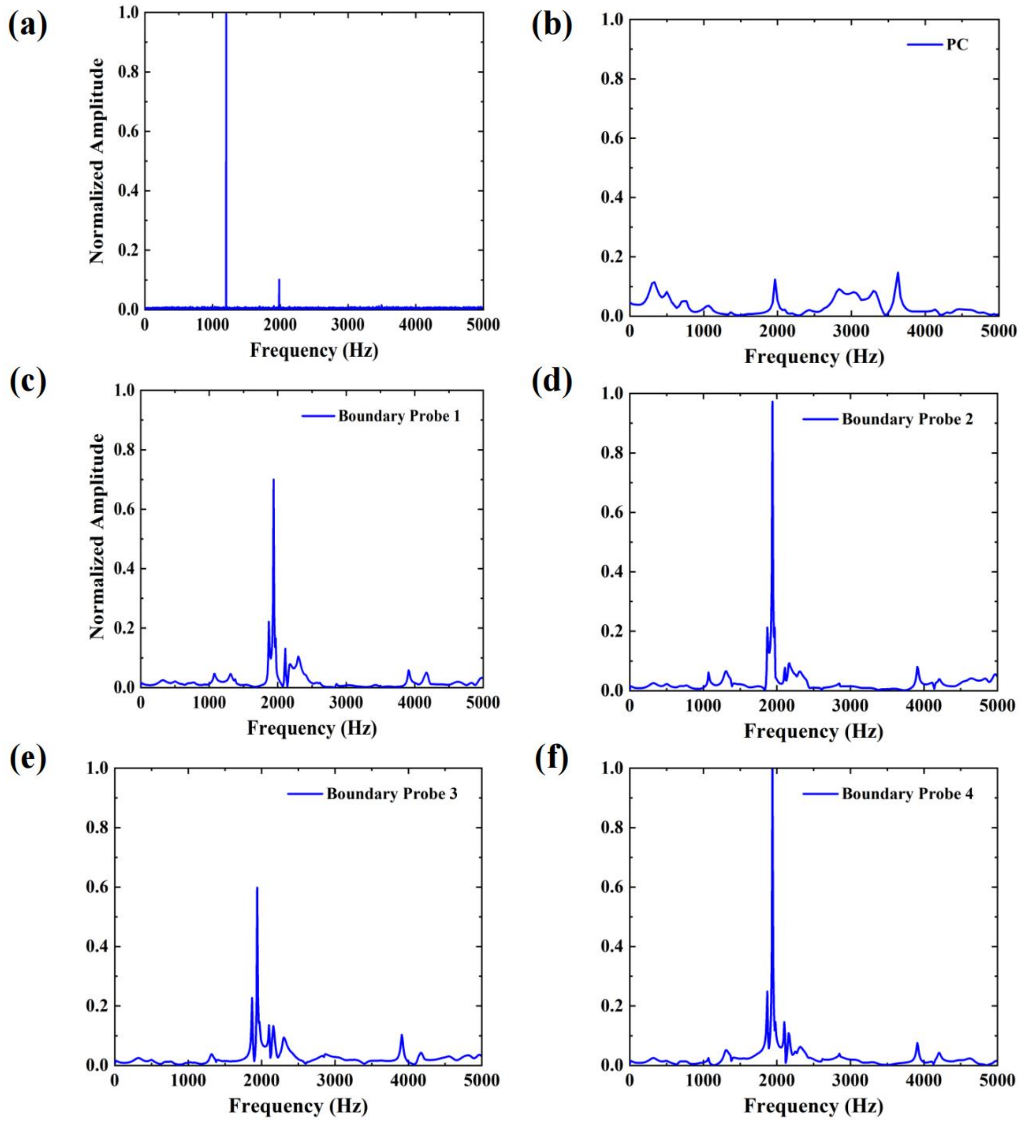

Figure 8. Frequency domain diagram of various signals: (**a**) harmonic signal. (**b**) PC point defect position signal. (**c**) Mies probe 1 position signal. (**d**) Mies probe 2 position signal. (**e**) Mies probe 3 position signal. (**f**) Mies probe 4 position signal.

6. Conclusions

To address the difficulty of perceiving weak signals and low SNR in traditional transducers, this paper proposes a PC-Mie by coupling PC defect states and Mies, which significantly amplifies the amplitude of the target frequency weak signals. The frequency domain analysis of the harmonic signal is evaluated and verified through practical experiments. The specific conclusions are as follows:

(1) The PC-Mie structure exhibits superior sound pressure enhancement performance when compared to either PC defect state structure or Mies. The pressure amplitude can be amplified over 700 times within the PC-Mies. This characteristic helps overcome the detection limits of traditional acoustic sensing systems.

(2) The capacity to amplify sound pressure amplitude is contingent upon the angle and location of the Mies at the center. The sound pressure detected by the probe inside the Mies increases as its position approaches the center of the localized sound field. Conversely, as the position of the Mies diverges from the center of the localized sound field, the sound pressure detected by the probe inside the structure decreases.

(3) Through testing and numerical calculations, it is found that the PC-Mie structure has a narrower bandwidth, making it more frequency-selective. Moreover, the resonant frequency of the Mies can be controlled by adjusting its model characteristics, thereby affecting the operating frequency of the PC-Mie structure. This property favors the structure as a superior adjustable bandpass amplifier for practical applications.
(4) Finally, the experiments verify that the PC-Mie structure can be used as an enhanced acoustic device or sensor for detecting harmonic signals, making it easier to detect weak signals. Although the acoustic enhancement and directional sensing of the PC-Mie structure may be limited by the narrow resonant frequency in practical applications, it is still applicable to most emergency sound detections. Acoustic device designed based on the coupling concept also opens up a new prospect for achieving high sensitivity and adjustability in acoustic sensing.

Author Contributions: Conceptualization, J.H.; methodology, G.H.; software, X.Z.; validation, J.H.; formal analysis, W.Y. and X.Z.; investigation, G.H.; resources, J.H.; data curation, W.Y. and X.Z.; writing—original draft preparation, J.H.; writing—review and editing, X.Z.; visualization, G.H.; supervision, J.H. and X.Z.; project administration, J.H. and X.Z.; funding acquisition, J.H. All authors have read and agreed to the published version of the manuscript.

Funding: This research was funded by National Key R&D Program of China, grant number 2023YFE0202800, Natural Science Foundation of Shanxi Province, grant number 202103021224201, and The National Natural Science Foundation of China, grant number 61671414.

Data Availability Statement: The data presented in this study are openly available in web of science.

Acknowledgments: The work was supported by National Key R&D Program of China, (2023YFE0202800), Natural Science Foundation of Shanxi Province (202103021224201) and The National Natural Science Foundation of China (61671414).

Conflicts of Interest: The authors declare no conflict of interest. The funders had role in the writing of the manuscript and in the decision to publish the results.

References

1. Miniaci, M.; Gliozzi, A.S.; Morvan, B.; Krushynska, A.; Bosia, F.; Scalerandi, M.; Pugno, N.M. Proof of Concept for an Ultrasensitive Technique to Detect and Localize Sources of Elastic Nonlinearity Using Phononic Crystals. *Phys. Rev. Lett.* **2017**, *118*, 214301. [CrossRef] [PubMed]
2. Danawe, H.; Okudan, G.; Ozevin, D.; Tol, S. Conformal gradient-index phononic crystal lens for ultrasonic wave focusing in pipe-like structures. *Appl. Phys. Lett.* **2020**, *117*, 021906. [CrossRef]
3. Li, Y.; Zhang, Y.P.; Dong, X.T.; Wang, H.Z. An attention-guided convolution neural network for denoising of distributed acoustic sensing-vertical seismic profile data. *Geophys. Prospect.* **2023**, *71*, 914–930. [CrossRef]
4. Lu, W.; Zhang, S.; Wang, R.X.; Xu, B.Q.; Yilmaz, M.; Zhang, W.D. Theoretical and Simulation Studies on Designing a Phase-Reversal-Based Broadband CMUT With Flat Passband and Improved Noise Rejections for SHM. *IEEE Sens. J.* **2022**, *22*, 21527–21539. [CrossRef]
5. Papila, M.; Haftka, R.T.; Nishida, T.; Sheplak, M. Piezoresistive microphone design Pareto optimization: Tradeoff between sensitivity and noise floor. *J. Microelectromech. Syst.* **2006**, *15*, 1632–1643. [CrossRef]
6. Zhang, S.; Lu, W.; Yang, Y.; Wang, R.; Zhang, G.; Xu, B.; Yilmaz, M.; Zhang, W. In-Plane-Sensing Analysis of Comb-Like Capacitive Micro-Machined Ultrasonic Transducers (CMUTs) Using Analytical Small-Signal Model and FEM. *IEEE Sens. J.* **2023**, *23*, 11498–11511. [CrossRef]
7. Liu, Y.Y.; Zhao, D.L.; Yan, Z.M.; Sun, W.P.; Guo, P.C.; Tan, T. Reprogrammable acoustic metamaterials for multiband energy harvesting. *Eng. Struct.* **2023**, *288*, 116207. [CrossRef]
8. Zhu, J.; Christensen, J.; Jung, J.; Martin-Moreno, L.; Yin, X.; Fok, L.; Zhang, X.; Garcia-Vidal, F.J. A holey-structured metamaterial for acoustic deep-subwavelength imaging. *Nat. Phys.* **2011**, *7*, 52–55. [CrossRef]
9. Hu, C.J.; Xue, S.W.; Yin, Y.H.; Hao, Z.L.; Zhou, Y.Y.; Chen, H.Y. Acoustic super-resolution imaging based on solid immersion 3D Maxwell's fish-eye lens. *Appl. Phys. Lett.* **2022**, *120*, 192202. [CrossRef]
10. Dahmani, H.; Smagin, N.; Campistron, P.; Carlier, J.; Toubal, M.; Nongaillard, B. One-channel time reversal focusing of ultra-high frequency acoustic waves on a MEMS. *Appl. Phys. Lett.* **2023**, *122*, 102201. [CrossRef]
11. Zangeneh-Nejad, F.; Fleury, R. Acoustic Analogues of High-Index Optical Waveguide Devices. *Sci. Rep.* **2018**, *8*, 10401. [CrossRef]

12. Sun, J.H.; Wu, T.T. Propagation of surface acoustic waves through sharply bent two-dimensional phononic crystal waveguides using a finite-difference time-domain method. *Phys. Rev. B* **2006**, *74*, 174305. [CrossRef]
13. Dai, H.Q.; Liu, T.T.; Xia, B.Z.; Yu, D.J. Quasilossless acoustic transmission in an arbitrary pathway of a network. *Phys. Rev. B* **2017**, *95*, 054109. [CrossRef]
14. Comandini, G.; Khodr, C.; Ting, V.P.; Azarpeyvand, M.; Scarpa, F. Sound absorption in Hilbert fractal and coiled acoustic metamaterials. *Appl. Phys. Lett.* **2022**, *120*, 061902. [CrossRef]
15. Zhao, X.S.; Han, J.N.; Yang, P.; Zhao, R.R. Research on High-Efficiency Transmission Characteristics of Multi-Channel Breast Ultrasound Signals Based on Graphene Structure. *Crystals* **2021**, *11*, 507. [CrossRef]
16. Gric, T. Tunable terahertz structure based on graphene hyperbolic metamaterials. *Opt. Quantum Electron.* **2019**, *51*, 202. [CrossRef]
17. Othman, M.A.K.; Guclu, C.; Capolino, F. Graphene–dielectric composite metamaterials: Evolution from elliptic to hyperbolic wavevector dispersion and the transverse epsilon-near-zero condition. *J. Nanophotonics* **2013**, *7*, 073089. [CrossRef]
18. Iorsh, I.V.; Mukhin, I.S.; Shadrivov, I.V.; Belov, P.A.; Kivshar, Y.S. Hyperbolic metamaterials based on multilayer graphene structures. *Phys. Rev. B* **2013**, *87*, 075416. [CrossRef]
19. Othman, M.A.; Guclu, C.; Capolino, F. Graphene-based tunable hyperbolic metamaterials and enhanced near-field absorption. *Opt. Express* **2013**, *21*, 7614–7632. [CrossRef]
20. Chang, Y.C.; Liu, C.H.; Liu, C.H.; Zhang, S.Y.; Marder, S.R.; Narimanov, E.E.; Zhong, Z.H.; Norris, T.B. Realization of mid-infrared graphene hyperbolic metamaterials. *Nat. Commun.* **2016**, *7*, 10568. [CrossRef]
21. Page, J.H.; Sukhovich, A.; Yang, S.; Cowan, M.L.; Van Der Biest, F.; Tourin, A.; Fink, M.; Liu, Z.; Chan, C.T.; Sheng, P. Phononic crystals. *Phys. Status Solidi (B)* **2004**, *241*, 3454–3462. [CrossRef]
22. Liang, Z.X.; Li, J.S. Extreme Acoustic Metamaterial by Coiling Up Space. *Phys. Rev. Lett.* **2012**, *108*, 114301. [CrossRef]
23. Kushwaha, M.S.; Halevi, P.; Dobrzynski, L.; Djafari-Rouhani, B. Acoustic band structure of periodic elastic composites. *Phys. Rev. Lett.* **1993**, *71*, 2022–2025. [CrossRef]
24. Ji, H.L.; Liang, Y.K.; Qiu, J.H.; Cheng, L.; Wu, Y.P. Enhancement of vibration based energy harvesting using compound acoustic black holes. *Mech. Syst. Signal Process.* **2019**, *132*, 441–456. [CrossRef]
25. Chen, T.G.; Jiao, J.R.; Yu, D.J. Strongly coupled phononic crystals resonator with high energy density for acoustic enhancement and directional sensing. *J. Sound Vib.* **2022**, *529*, 116911. [CrossRef]
26. Yang, A.C.; Lu, C.J.; Wu, F.Y.; Wu, Y.; Zhu, L.; Pei, M.L.; Liu, P.; Li, M.; Dai, X.M. Extremely-huge wave localization in coupled multilayer heterogeneous phononic crystal resonators. *Appl. Phys. Express* **2019**, *12*, 017001. [CrossRef]
27. Yang, A.C.; Li, P.; Wen, Y.M.; Lu, C.J.; Peng, X.; Zhang, J.T.; He, W. Enhanced Acoustic Energy Harvesting Using Coupled Resonance Structure of Sonic Crystal and Helmholtz Resonator. *Appl. Phys. Express* **2013**, *6*, 127101. [CrossRef]
28. Gao, D.; Zeng, X.; Liu, X.; Han, K.J. Resonant Modes of One-Dimensional Metamaterial Containing Helmholtz Resonators with Point Defect. *J. Mod. Phys.* **2017**, *8*, 1737–1747. [CrossRef]
29. Wu, F.; Hou, Z.; Liu, Z.; Liu, Y.J.P.L.A. Point defect states in two-dimensional phononic crystals. *Phys. Lett. A* **2001**, *292*, 198–202. [CrossRef]
30. Zhu, H.; Semperlotti, F.J.A.A. Metamaterial based embedded acoustic filters for structural applications. *AIP Adv.* **2013**, *3*, 092121. [CrossRef]
31. He, Y.; Wu, F.; Yao, Y.; Zhang, X.; Mu, Z.; Yan, S.; Cheng, C. Effect of defect configuration on the localization of phonons in two-dimensional phononic crystals. *Phys. Lett. A* **2013**, *377*, 889–894. [CrossRef]
32. Qi, S.; Oudich, M.; Li, Y.; Assouar, B.J.A.P.L. Acoustic energy harvesting based on a planar acoustic metamaterial. *Appl. Phys. Lett.* **2016**, *108*, 114905. [CrossRef]
33. Oudich, M.; Li, Y. Tunable Sub-wavelength Acoustic Energy Harvesting with Metamaterial Plate. *J. Phys. D Appl. Phys.* **2017**, *50*, 315104. [CrossRef]
34. Sun, H.X.; Fang, X.; Ge, Y.; Ren, X.D.; Yuan, S.Q. Acoustic focusing lens with near-zero refractive index based on coiling-up space structure. *Acta Phys. Sin.* **2017**, *66*, 244301. [CrossRef]
35. Zhang, T.; Bok, E.; Tomoda, M.; Matsuda, O.; Guo, J.; Liu, X.; Wright, O.B. Compact acoustic metamaterial based on the 3D Mie resonance of a maze ball with an octahedral structure. *Appl. Phys. Lett.* **2022**, *120*, 161701. [CrossRef]
36. Jia, Y.R.; Luo, Y.C.; Wu, D.J.; Wei, Q.; Liu, X.J. Enhanced Low-Frequency Monopole and Dipole Acoustic Antennas Based on a Subwavelength Bianisotropic Structure. *Adv. Mater. Technol.* **2020**, *5*, 1900970. [CrossRef]
37. Yao, J.; Ji, W.Q.; Wu, D.J.; Cheng, Y.; Liu, X.J. Plasmon-exciton couplings in Al-CuCl nanoshells and the effects of oxidation. *Opt. Commun.* **2017**, *389*, 310–313. [CrossRef]
38. Zhu, X.; Liang, B.; Kan, W.; Peng, Y.; Cheng, J. Deep-Subwavelength-Scale Directional Sensing Based on Highly Localized Dipolar Mie Resonances. *Phys. Rev. Appl.* **2016**, *5*, 054015. [CrossRef]
39. Chen, Y.; Liu, H.; Reilly, M.; Bae, H.; Yu, M. Enhanced acoustic sensing through wave compression and pressure amplification in anisotropic metamaterials. *Nat. Commun.* **2014**, *5*, 5247. [CrossRef]
40. Munday, J.N.; Bennett, C.B.; Robertson, W.M. Band gaps and defect modes in periodically structured waveguides. *J. Acoust. Soc. Am.* **2002**, *112*, 1353–1358. [CrossRef]

41. Zheng, K.; Li, T.L.; Su, Z.Q.; Zhang, B. Sparse Elitist Group Lasso Denoising in Frequency Domain for Bearing Fault Diagnosis. *IEEE Trans. Ind. Inform.* **2021**, *17*, 4681–4691. [CrossRef]
42. Li, Q.C.; Ding, X.X.; He, Q.B.; Huang, W.B.; Shao, Y.M. Manifold Sensing-Based Convolution Sparse Self-Learning for Defective Bearing Morphological Feature Extraction. *IEEE Trans. Ind. Inform.* **2021**, *17*, 3069–3078. [CrossRef]